Supplemental Material for

Nonequilibrium dynamics of Dirac quantum criticality in imaginary time

Yin-Kai Yu,[1,2,3,4] Zhi Zeng,[1,2] Yu-Rong Shu,[5] Zi-Xiang Li,[3,4,*] and Shuai Yin[1,2,†]

[1]*Guangdong Provincial Key Laboratory of Magnetoelectric Physics and Devices, Sun Yat-Sen University, Guangzhou 510275, China*
[2]*School of physics, Sun Yat-Sen University, Guangzhou 510275, China*
[3]*Beijing National Laboratory for Condensed Matter Physics & Institute of Physics, Chinese Academy of Sciences, Beijing 100190, China*
[4]*University of Chinese Academy of Sciences, Beijing 100049, China*
[5]*School of Physics and Materials Science, Guangzhou University, Guangzhou 510006, China*

(Dated: February 5, 2026)

CONTENTS

I. DETERMINANT QUANTUM MONTE CARLO

We employ the large-scale determinant quantum Monte Carlo (DQMC) method [1, 2] to investigate the imaginary-time relaxation dynamics of our model. Specifically, we prepare an initial state $|\psi_0\rangle$ and set the system parameters U/t on the critical point to observe the scaling behavior of observables during the short-time stage. When the system evolves to imaginary time τ, the expectation value of observables is given by

$$\langle O(\tau)\rangle = \frac{\langle\psi_0|\, \mathrm{e}^{-\frac{\tau}{2}H}\, O\, \mathrm{e}^{-\frac{\tau}{2}H}\, |\psi_0\rangle}{\langle\psi_0|\, \mathrm{e}^{-\tau H}\, |\psi_0\rangle}. \tag{S1}$$

Herein, the imaginary-time propagator acts on the initial state, projecting it closer to the ground state. Hence, the DQMC framework under this context is also termed propagator quantum Monte Carlo (PQMC). In numerical calculations, we use Trotter decomposition to discretize imaginary-time propagator into $M = \tau/\Delta\tau$ (M is integer) time slices with [3]

$$\mathrm{e}^{-\tau H} = \prod_{m=1}^{M}\left[\mathrm{e}^{-\Delta\tau H_t}\mathrm{e}^{-\Delta\tau H_U} + O\left(\Delta\tau^2\right)\right], \tag{S2}$$

* zixiangli@iphy.ac.cn
† yinsh6@mail.sysu.edu.cn

where H_t and H_U are the hopping term and Hubbard interaction term respectively in the Hamiltonian. We choose small enough $\Delta\tau/t < 0.05$. To decouple two-body fermion-fermion coupling form of $e^{\Delta\tau H_U}$, we use a discrete Hubbard-Stratonovich transformation [4, 5]

$$e^{-\frac{\Delta\tau U}{2}\left(n_{i\uparrow}+n_{i\downarrow}-1\right)^2} = \sum_{l=\pm1,\pm2} \gamma(l) e^{i\sqrt{\frac{\Delta\tau U}{2}}\eta(l)\left(n_{i\uparrow}+n_{i\downarrow}-1\right)}, \tag{S3}$$

to obtain one-body fermion-auxiliary field coupling. Here, we introduce a four-component space-time local auxiliary fields $\gamma(\pm1) = 1+\sqrt{6}/3, \gamma(\pm2) = 1-\sqrt{6}/3, \eta(\pm1) = \pm\sqrt{2\left(3-\sqrt{6}\right)}, \eta(\pm2) = \pm\sqrt{2\left(3+\sqrt{6}\right)}$, and use DQMC for importance sampling over these space-time configurations. Next, we elaborate on how DQMC numerically calculates the sampling weight.

For each imaginary time and each position of the Hubbard interaction, we employ an Hubbard-Stratonovich transformation as in Eq. (S3). This means that we introduce an auxiliary field in $d+1$ dimensions. As a result, the imaginary-time propagator can be fully expressed using single-particle operators. This allows us to represent it in the following quadratic form of fermion operators:

$$e^{-\tau H} \equiv \sum_c e^{-\tau H_c} = \sum_c A_c \prod_{m=1}^{M} e^{\vec{c}^\dagger T \vec{c}}\, e^{\vec{c}^\dagger V_{c(m)} \vec{c}}, \tag{S4}$$

where $\sum_c$ denotes the summation over all space-time configurations of the auxiliary field. Considering that each local component of the auxiliary field has 4 possible values, the summation comprises up to 4^{MN} terms, where N represents the number of spatial degrees of freedom. H_c denotes the decoupled configuration Hamiltonian, while T and $V_{c(m)}$ are the resulting quadratic coefficient matrices from the rearrangement, and A_c is the coefficient. Both $V_{c(m)}$ and A_c depend on the auxiliary field configuration. The complete form of the evolution operator has been presented above. Next, we consider expressing the initial state. The AFM, DSM, RS initial states we use are all direct product states, and numerically they can be written as the following Slater determinant:

$$|\psi_0\rangle = \bigotimes_{n_e=1}^{N_e} \left[\left(\sum_x c_x^\dagger P_{x,n_e}\right)|0\rangle\right] = \bigotimes_{n_e=1}^{N_e} \left[\left(\vec{c}^\dagger P\right)_{n_e}|0\rangle\right], \tag{S5}$$

where N_e denotes the number of electrons. This implies that the initial state is a direct product of N_e fermion single-particle wave functions. The index x denotes the degree of freedom of the electron, including spatial degrees of freedom, spin degrees of freedom, etc. The matrix element P_{x,n_e} represents the probability amplitude of the n_eth electron on the xth degree of freedom. Note that the imaginary-time propagator $e^{-\tau H_c}$ is essentially the Boltzmann weight factor of the auxiliary field configuration in statistical mechanics. According to Eqs. (S4) and (S5), the partition function of the auxiliary field configuration can be expressed as:

$$Z = \sum_c \langle\psi_0| e^{-\tau H_c} |\psi_0\rangle = \sum_c A_c \det\left[P^\dagger B_c(\tau,0) P\right]. \tag{S6}$$

Here, we use B_c to represent the exponential of the quadratic coefficient matrix:

$$B_c(\tau_2,\tau_1) \equiv \prod_{m=\tau_1/\Delta\tau}^{\tau_2/\Delta\tau} e^{T}\, e^{V_{c(m)}}. \tag{S7}$$

The expression on the right side of Eq. (S6) has integrated out the fermion operators, replacing the Grassmann numbers and fermion statistics, with a determinant representation that is computationally tractable. All matrix operations can be performed directly on a computer.

Ultimately, our Monte Carlo sampling is conducted over space-time configurations. Numerically, the weight of a space-time configuration is $A_c \det\left[P^\dagger B_c(\tau,0)P\right]$. Following the classical Markov importance sampling method, we continuously make tentative flips to the local components of this $d+1$ dimensional auxiliary field. We then employ the Metropolis algorithm to calculate the probability of accepting these changes based on the ratio of configuration weights before and after the flip. Specifically, we need to compute the following weight ratio:

$$R_{c'c} \equiv \frac{A_{c'} \det\left[P^\dagger B_{c'}(\tau,0)P\right]}{A_c \det\left[P^\dagger B_c(\tau,0)P\right]}, \tag{S8}$$

where c′ represents the flipped configuration and c represents the original configuration. In fact, we do not need to compute the weights of the two configurations separately. This is because the flipping we perform is localized in space-time, so

$$B_{c'}(\tau,0) = B_c(\tau,\zeta)\left(\mathbb{1}+\Delta_{c'c}\right)B_c(\zeta,0). \tag{S9}$$

Here, $\Delta_{c'c}$ is a highly sparse matrix, where only the matrix elements corresponding to the degrees of freedom involved in the local auxiliary field flipping are non-zero. Thus, the ratio of the two determinants can be expressed as:

$$\frac{\det\left[P^\dagger B_{c'}(\tau,0)P\right]}{\det\left[P^\dagger B_c(\tau,0)P\right]} = \det\left\{\mathbb{1} + \Delta_{c'c}B_c(\zeta,0)P\left[P^\dagger B_c(\tau,0)P\right]^{-1}P^\dagger B_c(\tau,\zeta)\right\}. \tag{S10}$$

Due to the sparsity of $\Delta_{c'c}$, the determinant on the right side of the above equation only requires consideration of a few degrees of freedom involved in the flipping during computations.

In DQMC, to compute the physical observables, we only need to statistically analyze the configurational observable $\langle O(\tau)\rangle_c$.

$$\langle O(\tau)\rangle = \sum_c \Pr_c \langle O(\tau)\rangle_c + \mathcal{O}\left(\Delta\tau^2\right), \tag{S11}$$

where $\Pr_c$ represents the configuration probability,

$$\Pr_c = \frac{1}{Z}A_c \det\left[P^\dagger B_c(\tau,0)P\right], \tag{S12}$$

$$\langle O(\tau)\rangle_c = \frac{\langle\psi_0|\, e^{-\frac{\tau}{2}H_c}\, O\, e^{-\frac{\tau}{2}H_c}\,|\psi_0\rangle}{\langle\psi_0|\, e^{-\tau H_c}\,|\psi_0\rangle}. \tag{S13}$$

Since we employ importance sampling, the sampling frequency is proportional to the configuration probability. Ultimately, when calculating the observable, we simply take the average over the sampled configurational observables. If the observable is a single-particle operator, meaning it can be expressed as a quadratic form of fermion operators, then one can integrate out the fermion degrees of freedom in a manner similar to Eq. (S6) and numerically compute using determinants. For observables of four-fermion operators or higher, we compute using the fermion equal-time Green's function based on Wick's theorem. After numerically integrating out the fermion degrees of freedom, the fermion equal-time Green's function can be expressed using the following matrix element:

$$\langle c^\dagger_{x_1} c_{x_2}\rangle_c = \left\{B_c\left(\frac{\tau}{2},0\right)P\left[P^\dagger B_c(\tau,0)P\right]^{-1}P^\dagger B_c\left(\tau,\frac{\tau}{2}\right)\right\}_{x_1,x_2}. \tag{S14}$$

II. DETERMINATION OF THE CRITICAL POINT

Here we offer supplementary details and numerical insights on pinpointing the critical point. In Fig. 2 (a) of the main text, we show that curves of R versus U for different sizes intersect at the critical point when τL^{-z} is taken as 0.3, 0.34, and 0.5. However, due to finite size effects, there may be slight deviations between the intersection points of small-sized curves and the real critical point. We denote the intersection points of size L and $L+3$ as $U_c(L)$, which are shown in Fig. S1.

We extrapolate the critical point in thermodynamic limit $L \to \infty$ using the form $U_c(L) = U_c + aL^{-w}$. The intercept shown in Fig. S1 represents the extrapolated critical point. For three different cases of $\tau L^{-z} = 0.3$, 0.34, and 0.5, our results are $U_c = 3.91(3)$, 3.92(1), and 3.88(4) respectively. They all extrapolate to the same limit within the error range, thus demonstrating that our method based on nonequilibrium information to determine critical point in fermion criticality is reliable.

It is worth mentioning that as shown in Fig. S1, the $U_c(L)$ approaches the critical point with different trends as L increases for different values of τ/L. Specifically, when $\tau/L = 0.3$, the $U_c(L)$ under small size is smaller than the real critical point at thermodynamic limit; while when $\tau/L = 0.5$, the $U_c(L)$ under small size is larger than the real critical point. More interestingly, we found that at $\tau/L = 0.34$, the $U_c(L)$ almost does not depend on size and can exhibit a real critical behavior under small sizes alone. These results demonstrate that our method is quite reliable in determining the critical point.

III. MORE RESULTS ABOUT THE CRITICAL EXPONENTS

A. The correlation length exponent ν

In the main text, we use the data with fixed $\tau L^{-z} = 0.3$ to determine the critical exponent ν. Here, we supplement the results of $\tau L^{-z} = 0.5$ and 0.34. Fig. S2 shows the curves of different sizes' correlation-length ratios changing with U/t. We adjust the rescaling parameters U_c and ν to make the curves of different sizes coincide. To avoid finite size effects as much as possible, we fit U_c and ν using curves above $L = 12$. For $\tau L^{-z} = 0.5$ and 0.34, we obtain results of $U_c = 3.91(2)$ and 3.92(4), respectively, as

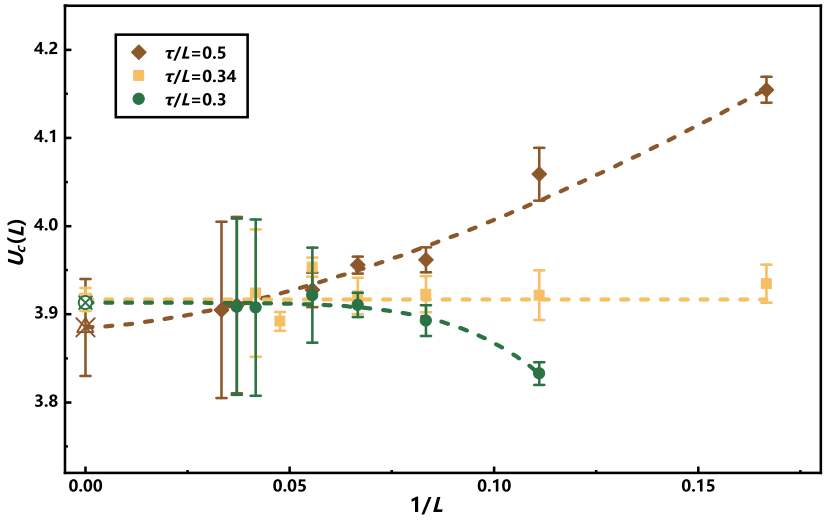

FIG. S1. Determine the critical point by extrapolation. When τL^{-z} is fixed at 0.3, 0.34, and 0.5 respectively, the intersection points $U_c(L)$ of the curves of R versus U for sizes L and $L+3$ are shown in the figure. The critical point is extrapolated when the system tends to thermodynamic limit $L \to \infty$. Note that the extrapolation results are also marked at $1/L = 0$.

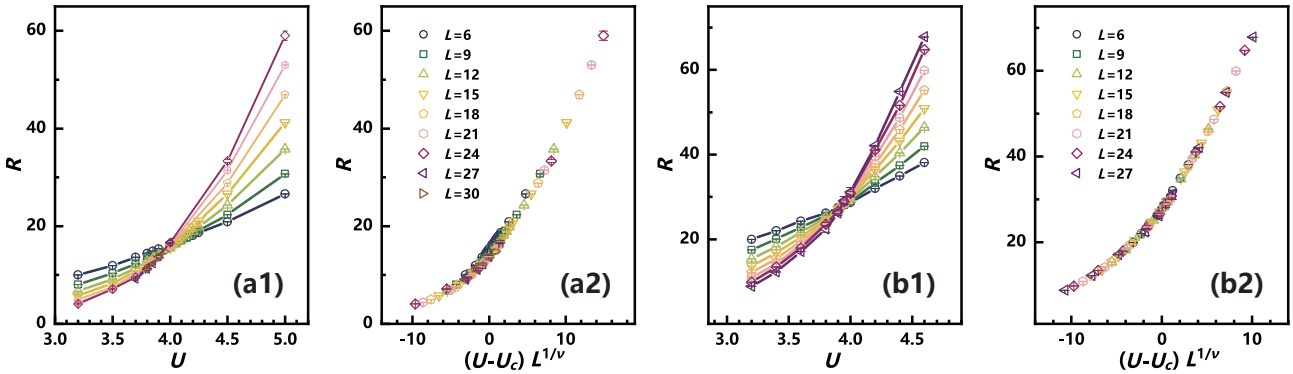

FIG. S2. The variation of the correlation-length ratio with respect to U/t at fixed τL^{-z}. (a1) display the results obtained by setting $\tau L^{-z} = 0.5$. (a2) shows rescaling is applied to the horizontal axis of (a1). (b1) display the results obtained by setting $\tau L^{-z} = 0.34$. (b2) shows rescaling is applied to the horizontal axis of (b1).

well as $\nu = 1.22(6)$ and $1.22(17)$. They are consistent with our results presented in the main text, and consistent with the previous results of equilibrium systems within error range [6].

Moreover, by using these results for rescaling, in Fig. S2 (a2), we find that for $\tau L^{-z} = 0.5$, curves for small L do not completely coincide with large-size curves; while in Fig. S2 (b2), it is shown that all curves can coincide very well for $\tau L^{-z} = 0.34$. These results are consistent with the drift of $U_c(L)$ found in the previous section.

B. The dynamic exponent z

In the main text, we directly set the dynamic exponent z as $z = 1$, which is based on the Lorentz symmetry of effective theory of the Dirac criticality. Here we show that the dynamic exponent z can be determined independently.

To do this, we define the ratio of m^2 for the DSM and AFM initial states as $R_m \equiv m^2_{\mathrm{DSM}}/m^2_{\mathrm{AFM}}$. At the critical point, according to Eqs. (4) and (7) in the main text, one finds that R_m satisfies the scaling form

$$R_m(\tau, L) = L^{-d}\tau^{d/z} f_{R_m}(\tau L^{-z}). \tag{S15}$$

In this scaling function, $d = 2$ and z is the only independent critical exponent.

Based on Eq. (S15), there are two approaches to determine z:

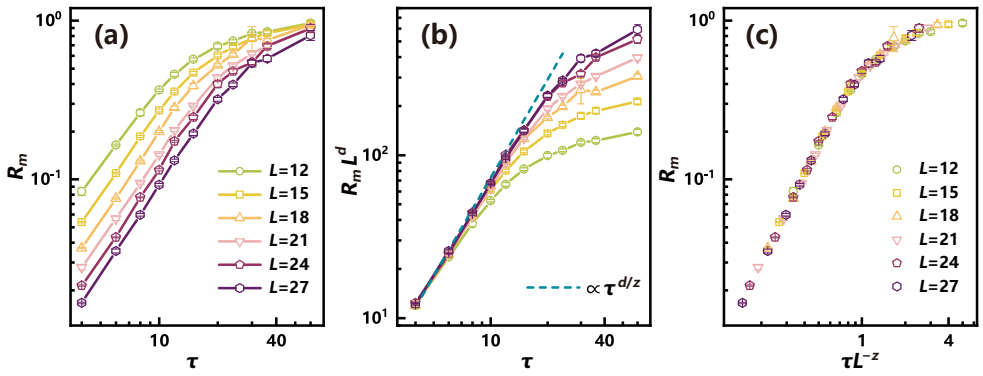

FIG. S3. Evolution of R_m for different sizes L. (a) Curves of R_m versus τ at the critical point for different sizes (b) For small τ, R_m obeys $R_m L^d \sim \tau^{d/z}$ for different sizes. The dashed line with $z = 1$ is plotted for comparison. (c) By rescaling the imaginary time τ as τL^{-z}, data collapse fitting yields $z = 1.01(9)$.

(a) In the short-time stage, f_{Rm} only weakly depends on L. So, R_m in the short-time stage should satisfy

$$R_m(\tau, L) \propto L^{-d}\tau^{d/z}. \tag{S16}$$

Figure S3 (a) shows the evolution of R_m for different size L. By rescaling R_m as $R_m L^d$, Fig. S3 (b) confirms that f_{Gm} only weakly depends on L in the short-time stage. Then, we directly fit the curve for largest size in the short-time range according to Eq. (S16) and find that $z = 1.07(1)$, which is close to the exact result with $z = 1$.

(b) A more accurate method is to adjust the value of z for the rescaled curves of $R_m = L^{-d}\tau^{d/z}$ versus τL^{-z} according to Eq. (S15) to make curves of different sizes collapse with each other, yielding the value of z as $z = 1.01(9)$, as shown in Fig. S3 (c).

Although for the model studied in this paper, the dynamic exponent $z = 1$ can be obtained from the Lorentz symmetry of the effective Hamiltonian, determining z independently is also crucial. First, we can examine the effective field theory for the microscopic model. Second, in estimation of the critical point, we fix τL^{-z} to be a constant with $z = 1$. Determining z at the critical point gives a consistent examination of the procedure.

IV. DYNAMIC SCALING OF m^2 AND G FROM RANDOM-SPIN INITIAL STATE

In the main text, for the random-spin (RS) initial state, we only focus on the critical initial slip behaviors. Here we investigate the imaginary-time critical dynamics of the square of the order parameter m^2 and the fermion correlation function G.

At first, we show that m^2 obeys

$$m^2(\tau, L) = L^{-d}\tau^{d/z-2\beta/\nu z} f_{m3}(\tau L^{-z}), \tag{S17}$$

which is similar to Eq. (7). This is because both RS and DSM states are disordered for the magnetic order. Figure S4 (a1) shows the evolution of m^2 for different L. From Fig. S4 (a1), one finds that in the short-time stage, $m^2 \propto L^{-d}\tau^{d/z-2\beta/\nu z}$. By rescaling m^2 and τ as $m^2 L^{2\beta/\nu z}$ and τL^{-z}, respectively, with the critical exponents determined in the main text, Fig. S4 (a2) shows that the rescaled curves collapse onto a single curve, confirming Eq. (S17) and the values of the critical exponents.

Then, we turn to explore the scaling behavior of $G(\Delta \boldsymbol{q})$. We find that G satisfies

$$G(\tau, L) = L^{-z}\tau^{1-\eta_\psi/z} f_{G2}(\tau L^{-z}), \tag{S18}$$

which is similar to Eq. (7). This is because both RS and Mott insulator states are gapped phase for the fermion particles. Figure S4 (b1) shows the evolution of G for different L. In the short-time stage, the curve of G versus τ is consistent with $G \propto \tau^{1-\eta_\psi/z}$. Moreover, by rescaling G and τ as GL^{η_ψ} and τL^{-z}, respectively, with $\eta_\psi = 0.15(4)$ determined in the main text, we find in Fig. S4 (b2) that the rescaled curves collapse onto each other, confirming not only Eq. (S18) but also the value of η_ψ.

Combining the scaling forms of the square of the order parameter m^2 and G, we find interesting results that scaling forms of m^2 for the DSM and RS initial states are similar; whereas scaling forms of G for AFM and RS initial states are similar. These results provide further crosscheck for the critical exponents determined via nonequilibrium methods.

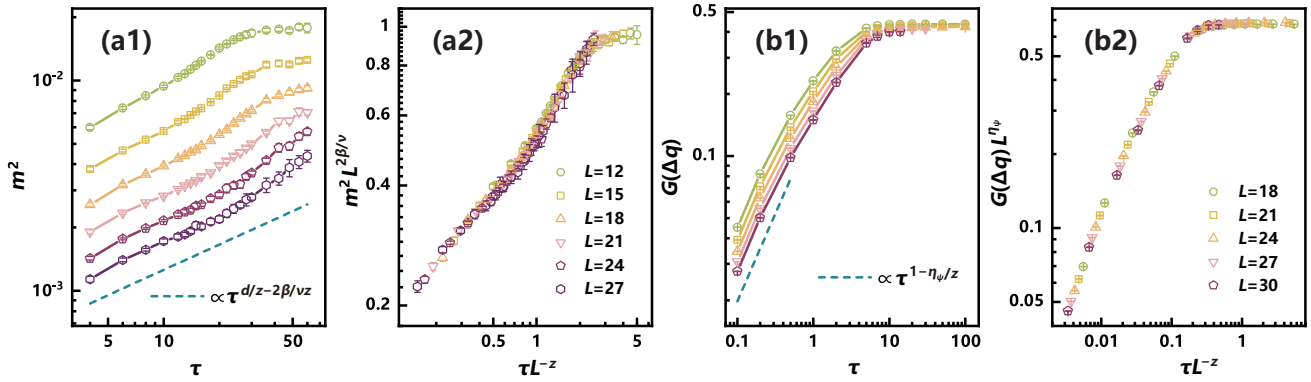

FIG. S4. Relaxation dynamics of order paremeter m^2 and fermion correlation $G(\Delta \boldsymbol{q})$ with the RS initial state. Curves of m^2 versus τ at the critical point for different sizes before (a1) and after (a2) rescaling. The dashed line in (a1) representing $m^2 \propto \tau^{-2\beta/\nu z}$ with $\beta/\nu = 0.80$ estimated from the main text is plotted for comparison. Curves of $G(\Delta \boldsymbol{q})$ versus τ at the critical point for different sizes before (b1) and after (b2) rescaling. The dashed line in (b1) representing $G(\Delta \boldsymbol{q}) \propto \tau^{1-2\eta_\psi/z}$ with $\eta_\psi = 0.15(4)$ estimated from the main text is plotted for comparison.

V. CRITICAL INITIAL SLIP

A. Critical initial slip in the order parameter

In the main text, we unveil the critical initial slip via the scaling behavior of the auto-correlation function with the RS initial state. Actually, the critical initital slip exponent also manifests itself in the evolution of the order parameter m [7, 8].

To exhibit the critical initial slip in m, the initial state should be changed to the uncorrelated initial state with a very small magnetization m_0. Under this condition, m evolves as [7, 8]

$$m = \tau^{-\frac{\beta}{\nu z}} f_{m4}(m_0 \tau^{\theta+\beta/\nu z}). \tag{S19}$$

Here we at first focus on the thermodynamic limit. Expanding m_0 in f_{m4} gives the leading term of m as

$$m \propto m_0 \tau^{\theta}. \tag{S20}$$

When m_0 becomes larger, the rescaled scaling variable $m_0 \tau^{\theta+\beta/\nu z}$ becomes invalid. Instead, a universal characteristic function should be introduced. For this case, the evolution in the initial stage no longer demonstrates power behavior [9, 10]. These scaling behaviors have been found in both classical relaxation dynamics and quantum imaginary-time relaxation dynamics.

For classical systems, in general, θ is positive. Thus, in the initial stage, the order parameter increases, rather than directly decays to its equilibrium value $m = 0$. The reason for this critical initial slip behavior is the competition between the domain formation and the critical fluctuations. The former describes the tendency that the local spin always wants to make its neighbors orient along the same (for ferromagnetic case)/inverse (for antiferromagnetic) direction, thus forming the magnetic domain; while the latter describes the destruction of the order by strong fluctuations near the critical point. In equilibrium, the latter dominates and $m = 0$ at the critical point. However, since the initial state is an uncorrelated state, from which critical fluctuations should increase from infancy. Thus, in the early stage, the domain formation dominates and m increases. As time goes on, the critical fluctuations becomes strong enough to destroy the order, and m begin to decay as $m \propto \tau^{-\beta/\nu z}$.

However, in the present case, from Fig. S4, we find that the fermion correlation function always tends to its equilibrium value much faster than the order parameter. Thus, gapless Dirac fermions can contribute significant critical fluctuations to prevent the domain formation, making θ negative.

Although m also contains the information of θ, here it is very difficult to obtain θ from the scaling of m in Monte Carlo simulation. The reason is that the scaling relation $m \propto m_0 \tau^{\theta}$ requires that m_0 should be very small. For finite-size systems employed in our manuscript, the smallest m_0 is $m_0 \sim L^{-2}$, which is too large to satisfy the condition. Moreover, for finite-size system, L should also be considered as a scaling variable. So, in our paper, we use the auto-correlation function from a random initial state to get the value of θ. This is also a usual method to obtain θ in classical systems [11].

B. θ for quantum Ising models

In the main text, we determine the critical initial slip exponent θ of the Dirac fermions through the critical relaxation behavior of the auto-correlation function A. Here, we study the critical dynamics of the auto-correlation function A in the 1D and 2D

transverse-field Ising models. In previous works [8, 12], the critical initial slip exponent for the 1D and 2D Ising models is obtained from other methods. Here, we show that the critical initial slip exponent for these models can also be obtained from the scaling of A. Fig. S5 (a1) shows the relaxation process of A for various sizes of the 1D transverse-field Ising model at the critical point $h/J = 1$. In Fig. S5 (a2), we rescale the relaxation process for 1D. Here, we take $\theta = 0.3734$ [12] and $z = 1$. After rescaling, the relaxation curves of different sizes overlap, satisfying the scaling relation for A as mentioned in our main text. For the 2D transverse-field Ising model at the critical point $h/J = 3.04451$, we performed similar numerical simulations, as shown in Fig. S5 (b1). The relaxation curves of various sizes of A overlap when rescaled with $\theta = 0.209$ [12], as shown in Fig. S5 (b2). Note that for both 1D and 2D quantum Ising models, the critical initial slip exponent is positive.

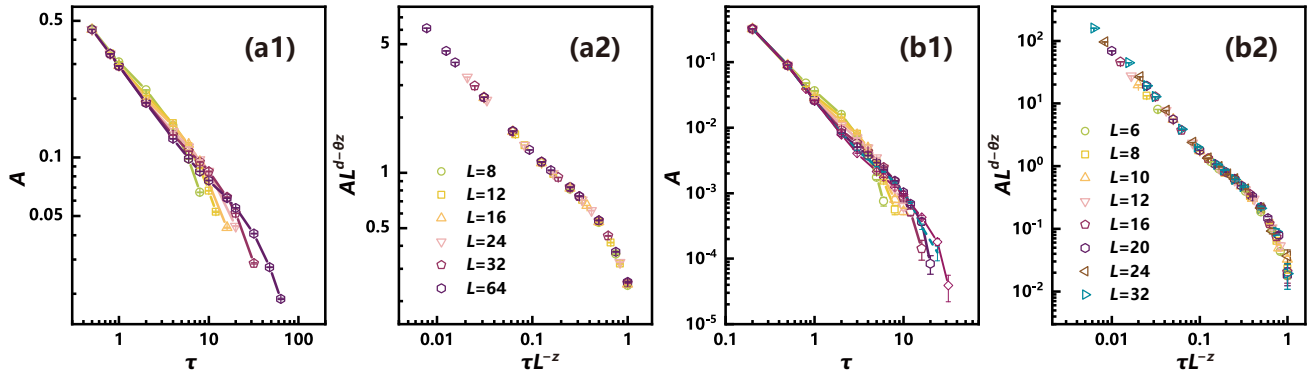

FIG. S5. The relaxation behavior of the auto-correlation function A in the quantum Ising model. (a1) and (b1) respectively show the results in 1D and 2D. (a2) and (b2) are their rescaled results, where the relaxation curves of different sizes overlap.

VI. OFF-CRITICAL-POINT EFFECTS

In the main text, after determining the critical point, we focus on the case with $g = 0$. Here, we discuss the off-critical-point effects.

A. Scaling forms with $g \neq 0$

When $g \neq 0$, the scaling functions should include $gL^{1/\nu}$ as an indispensable variable. Therefore, for the AFM initial state, the evolution of m^2 should satisfy

$$m^2(g, L, \tau) = \tau^{-2\beta/\nu z} f_{g1}(\tau L^{-z}, gL^{1/\nu}), \tag{S21}$$

which can be transformed to be $m^2(g, L, \tau) = L^{-2\beta/\nu} f_{g2}(\tau L^{-z}, gL^{1/\nu})$. Similarly, with the AFM initial state, the fermion correlation function G should satisfy

$$G(g, L, \tau) = L^{-z}\tau^{1-\eta_\psi/z} f_{g3}(\tau L^{-z}, gL^{1/\nu}), \tag{S22}$$

which is equivalent to $G(g, L, \tau) = L^{-\eta_\psi} f_{g4}(\tau L^{-z}, gL^{1/\nu})$ according to the scaling transformation.

In addition, for the DSM initial state, the evolution of m^2 should satisfy

$$m^2(g, L, \tau) = L^{-d}\tau^{d/z-2\beta/\nu z} f_{g5}(\tau L^{-z}, gL^{1/\nu}), \tag{S23}$$

which can be transformed to be $m^2(g, L, \tau) = L^{-2\beta/\nu} f_{g6}(\tau L^{-z}, gL^{1/\nu})$. Similarly, with the DSM initial state, the fermion correlation function G should satisfy

$$G(g, L, \tau) = L^{-z}\tau^{1-\eta_\psi/z} f_{g7}(\tau L^{-z}, gL^{1/\nu}), \tag{S24}$$

which is equivalent to $G(g, L, \tau) = L^{-\eta_\psi} f_{g8}(\tau L^{-z}, gL^{1/\nu})$.

B. Numerical Results

At first, we show the numerical results for the AFM initial state. For a fixed τL^{-z}, the scaling form of m^2 reduces to $m^2(g, L) = L^{-2\beta/\nu} f_{m2}(gL^{1/\nu})$. Fig. S6 depicts the dependence of m^2 on U for different system sizes at $\tau L^{-z} = 0.3$. By tuning the exponents to make the rescaled curves of m^2 versus g collapse, we determine the exponents as $\nu = 1.025(9)$ and $\beta/\nu = 0.735(2)$, as shown in Fig. S6 (b). These values are consistent with the previous results of equilibrium systems [13] and also consistent with the non-equilibrium results determined at QCP in our main text.

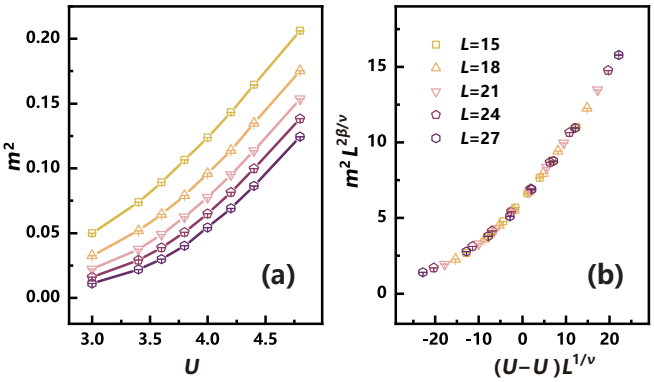

FIG. S6. Estimation of ν and β by scaling collapse analysis of m^2. Curves of m^2 versus U with fixed $\tau L^{-z} = 0.3$ before (a) and after (b) rescaling.

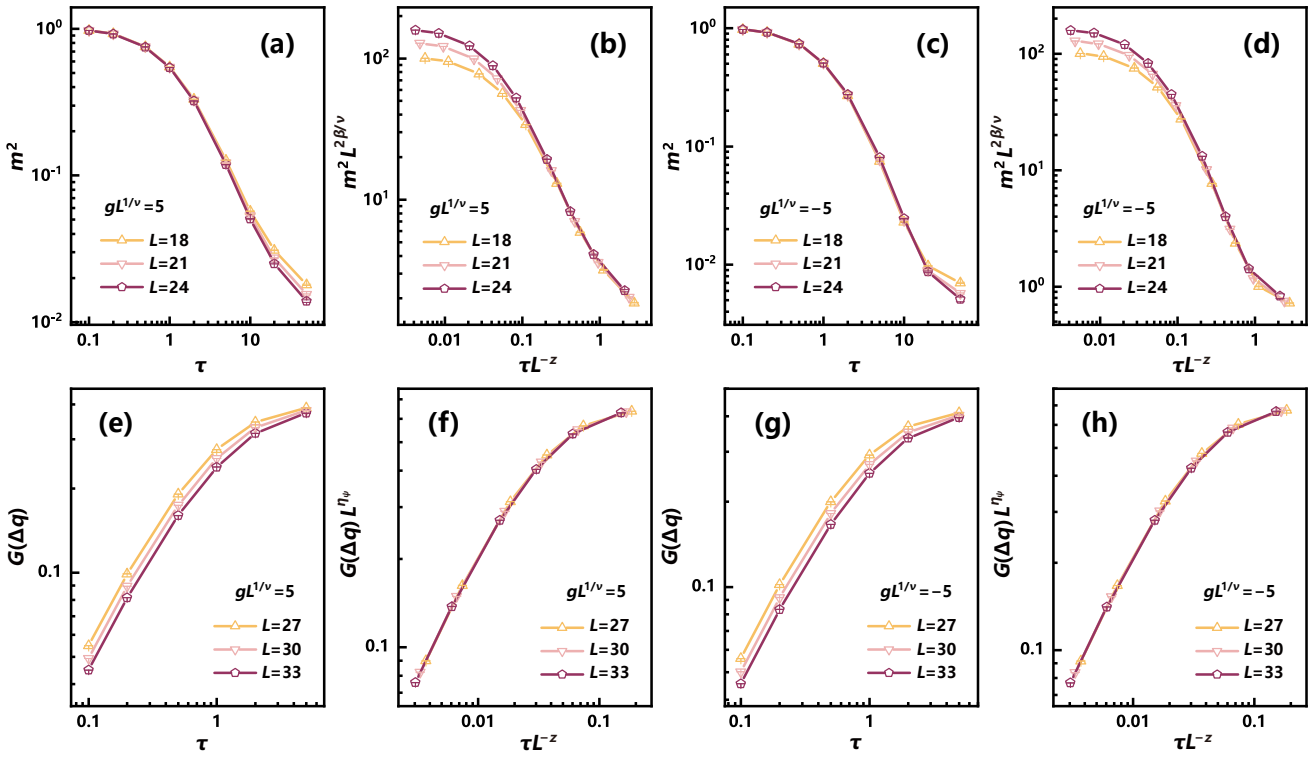

FIG. S7. Relaxation dynamics of m^2 and G from AFM initial state for $g \neq 0$.

In addition, by fixing $gL^{1/\nu}$, we explore the iamgianry-time relaxation dynamics of m^2 and G and show the results in Fig. S7. For both $gL^{1/\nu} = 5$ or $gL^{1/\nu} = -5$ (where $\nu = 1.025$ estimated from Fig. S6), we find that the rescaled curves of m^2 and G according to Eqs. (S21) and (S22), respectively, collapse onto each other quite well, confirming Eqs. (S21) and (S22).

Then we study the relaxation dynamics with DSM initial state. For both $gL^{1/\nu} = 5$ or $gL^{1/\nu} = -5$ (where $\nu = 1.025$), we find in Fig. S8 that the rescaled curves of m^2 collapse together according to Eq. (S23). In addtion, for both $gL^{1/\nu} = 5$ or $gL^{1/\nu} = -5$

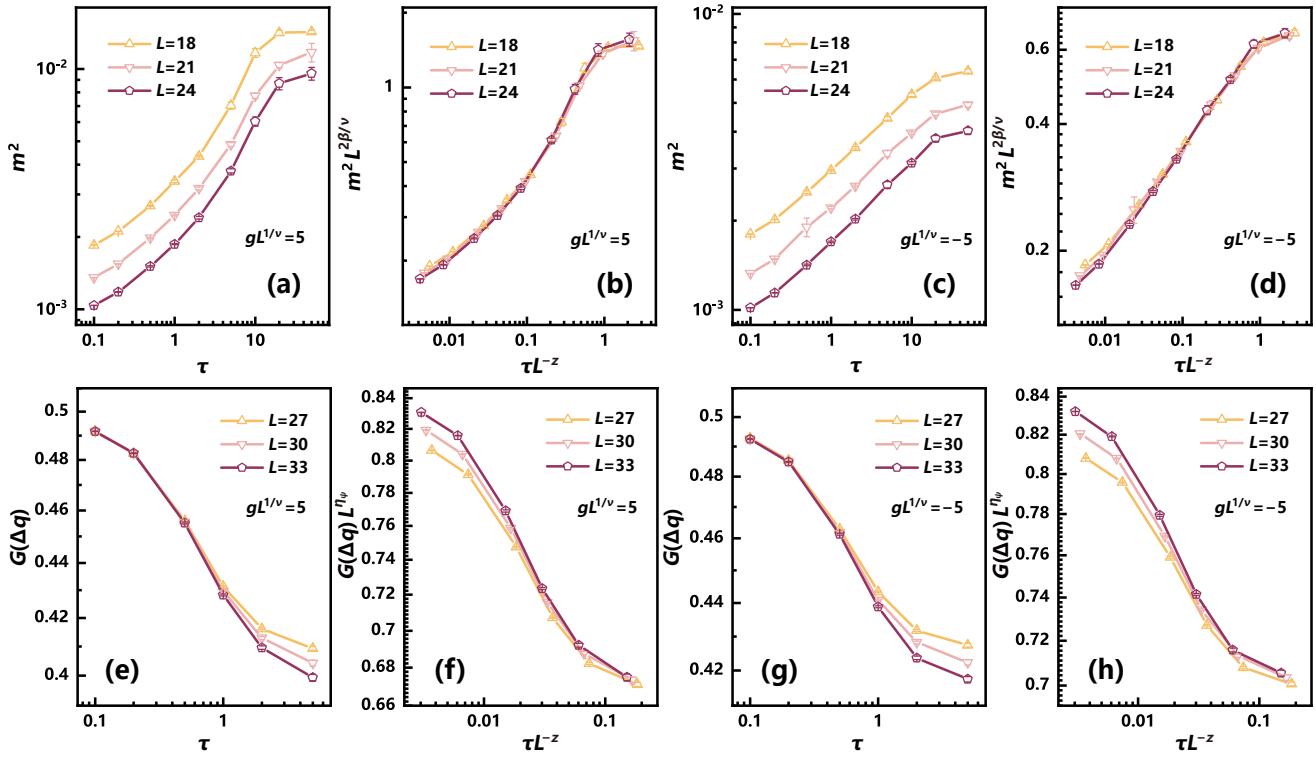

FIG. S8. Relaxation dynamics of m^2 and G from DSM initial state for $g \neq 0$.

with $\nu = 1.025$, the rescaled curves of G match with each other, confirming Eq. (S24).

VII. FERMION CORRELATION AND QUASI-PARTICLE WEIGHT

The quasi-particle weight Z characterizes fermionic single-particle excitations near the Fermi surface/Dirac point [14–17]. The relation between Z and the distribution function is

$$Z = \lim_{L\to\infty} [n(\varepsilon_{\boldsymbol{q}} = 0^-) - n(\varepsilon_{\boldsymbol{q}} = 0^+)], \tag{S25}$$

in which the energy resolved momentum distribution function is defined as

$$n(\varepsilon_{\boldsymbol{q}} = \pm|\varepsilon_{\boldsymbol{q}}|) = \langle \psi^\dagger_{\pm,\boldsymbol{q},\sigma}\psi_{\pm,\boldsymbol{q},\sigma}\rangle\,. \tag{S26}$$

$\psi_{\pm,\boldsymbol{q},\sigma}$ is the quasi-particle operator, with $+(-)$ indicating above (below) the Fermi surface/Dirac point, respectively, and σ being the spin index.

For the non-interacting case, the quasi-particle energy takes the eigenvalues of the Hamiltonian $\varepsilon_{\boldsymbol{q}} = \pm|h_{\boldsymbol{q}}|$, where $h_{\boldsymbol{q}} = -t(1 + \mathrm{e}^{-\mathrm{i}\boldsymbol{q}\cdot\boldsymbol{a}_1} + \mathrm{e}^{-\mathrm{i}\boldsymbol{q}\cdot\boldsymbol{a}_2})$ in honeycomb lattice, and the Hamiltonian can be written into diagonal representation:

$$H_0 = \sum_{\boldsymbol{q},\sigma} \begin{pmatrix} c^\dagger_{A,\boldsymbol{q},\sigma} & c^\dagger_{B,\boldsymbol{q},\sigma}\end{pmatrix} \begin{pmatrix} 0 & h_{\boldsymbol{q}} \\ h^*_{\boldsymbol{q}} & 0\end{pmatrix} \begin{pmatrix} c_{A,\boldsymbol{q},\sigma} \\ c_{B,\boldsymbol{q},\sigma}\end{pmatrix} = \sum_{\boldsymbol{q},\sigma} \begin{pmatrix} \psi^\dagger_{+,\boldsymbol{q},\sigma} & \psi^\dagger_{-,\boldsymbol{q},\sigma}\end{pmatrix} \begin{pmatrix} |h_{\boldsymbol{q}}| & 0 \\ 0 & -|h_{\boldsymbol{q}}|\end{pmatrix} \begin{pmatrix} \psi_{+,\boldsymbol{q},\sigma} \\ \psi_{-,\boldsymbol{q},\sigma}\end{pmatrix}, \tag{S27}$$

where the annihilation operators $\psi_{-,\boldsymbol{q},\sigma}$ and $\psi_{+,\boldsymbol{q},\sigma}$ of the bonding and anti-bonding states, respectively, are given as

$$\psi_{\pm,\boldsymbol{q},\sigma} = \frac{1}{\sqrt{2}}\left(c_{A,\boldsymbol{q},\sigma} \pm \frac{h_{\boldsymbol{q}}}{|h_{\boldsymbol{q}}|} c_{B,\boldsymbol{q},\sigma}\right). \tag{S28}$$

The orbital subscripts A, B represent the two sublattices in the honeycomb, and $c_{\alpha,\boldsymbol{q},\sigma}$ annihilation an electron on $\alpha = A, B$ sublattice:

$$c_{\alpha,\boldsymbol{q},\sigma} = \frac{1}{\sqrt{N}} \sum_{i_\alpha} \mathrm{e}^{-\mathrm{i}\boldsymbol{q}\cdot\boldsymbol{r}_i} c_{i_\alpha,\sigma}. \tag{S29}$$

Thus, the occupation in the non-interacting case simply reads:

$$\langle \psi^\dagger_{\pm,\boldsymbol{q},\sigma}\psi_{\pm,\boldsymbol{q},\sigma}\rangle = \frac{1}{2}\left(\langle c^\dagger_{A,\boldsymbol{q},\sigma}c_{A,\boldsymbol{q},\sigma}\rangle + \langle c^\dagger_{B,\boldsymbol{q},\sigma}c_{B,\boldsymbol{q},\sigma}\rangle\right) \pm \frac{1}{2}\left(\frac{h_{\boldsymbol{q}}}{|h_{\boldsymbol{q}}|}\langle c^\dagger_{A,\boldsymbol{q},\sigma}c_{B,\boldsymbol{q},\sigma}\rangle + \frac{h^*_{\boldsymbol{q}}}{|h_{\boldsymbol{q}}|}\langle c^\dagger_{B,\boldsymbol{q},\sigma}c_{A,\boldsymbol{q},\sigma}\rangle\right). \tag{S30}$$

Considering the non-interacting solution $\langle c^\dagger_{A,\boldsymbol{q},\sigma}c_{A,\boldsymbol{q},\sigma}\rangle = \langle c^\dagger_{B,\boldsymbol{q},\sigma}c_{B,\boldsymbol{q},\sigma}\rangle = \frac{1}{2}$, $\langle c^\dagger_{A,\boldsymbol{q},\sigma}c_{B,\boldsymbol{q},\sigma}\rangle^* = \langle c^\dagger_{B,\boldsymbol{q},\sigma}c_{A,\boldsymbol{q},\sigma}\rangle = -\frac{h_{\boldsymbol{q}}}{2|h_{\boldsymbol{q}}|}$ at half filling, the groud-state-occupation of the bonding and anti-bonding are respectively $\langle \psi^\dagger_{-,\boldsymbol{q},\sigma}\psi_{-,\boldsymbol{q},\sigma}\rangle = 1$ and $\langle \psi^\dagger_{+,\boldsymbol{q},\sigma}\psi_{+,\boldsymbol{q},\sigma}\rangle = 0$. Consequently, quasi-particle weight $Z = 1$.

For the case with interaction, $\langle c^\dagger_{A,\boldsymbol{q},\sigma}c_{A,\boldsymbol{q},\sigma}\rangle = \langle c^\dagger_{B,\boldsymbol{q},\sigma}c_{B,\boldsymbol{q},\sigma}\rangle = \frac{1}{2}$ for all momenta still holds due to the particle-hole symmetry at half-filling, and only off-diagonal correlation $\langle c^\dagger_{A,\boldsymbol{q},\sigma}c_{B,\boldsymbol{q},\sigma}\rangle^* = \langle c^\dagger_{B,\boldsymbol{q},\sigma}c_{A,\boldsymbol{q},\sigma}\rangle \equiv f_{\boldsymbol{q}}$ bears non-trivial fermion correlation. Therefore, the "dressed" quasi-particle operators in interacting case read (the same formula appears in Ref. [13]):

$$\psi_{\pm,\boldsymbol{q},\sigma} = \frac{1}{\sqrt{2}}\left(c_{A,\boldsymbol{q},\sigma} \pm \frac{f_{\boldsymbol{q}}}{|f_{\boldsymbol{q}}|}c_{B,\boldsymbol{q},\sigma}\right), \tag{S31}$$

with the occupation

$$\langle \psi^\dagger_{\pm,\boldsymbol{q},\sigma}\psi_{\pm,\boldsymbol{q},\sigma}\rangle = \frac{1}{2} \pm |f_{\boldsymbol{q}}|. \tag{S32}$$

Finally, one can use the fermion correlation near the Fermi surface (Dirac point K) to calculate the occupation jump (Ref. [15]):

$$Z = \lim_{L\to\infty} 2|f_{K+\Delta\boldsymbol{q}}| = \lim_{L\to\infty} 2|G(\Delta\boldsymbol{q})| \tag{S33}$$

where $G(\Delta\boldsymbol{q}) \equiv \frac{1}{L^d}\sum_{ij} \mathrm{e}^{\mathrm{i}(K+\Delta\boldsymbol{q})\cdot(\boldsymbol{r}_i-\boldsymbol{r}_j)}c^\dagger_{i,A}c_{j,B}$ is the fermion correlation we calculated in the main text, and $\Delta\boldsymbol{q}$ is the smallest lattice momentum. Due to the direct proportional relationship, the quasiparticle weight Z and the fermion correlation $G(\Delta\boldsymbol{q})$ have the same anomalous dimension η_ψ. In the thermodynamic limit, the DSM phase has $Z = 1$, meaning $G(\Delta\boldsymbol{q}) = 0.5$, while the AFM phase has $Z = 0$, with $G(\Delta\boldsymbol{q}) = 0$.

[1] F. Assaad and H. Evertz, World-line and determinantal quantum monte carlo methods for spins, phonons and electrons, in *Computational Many-Particle Physics* (Springer Berlin Heidelberg, Berlin, Heidelberg, 2008) pp. 277–356.

[2] F. F. Assaad, M. Bercx, F. Goth, A. Götz, J. S. Hofmann, E. Huffman, Z. Liu, F. P. Toldin, J. S. E. Portela, and J. Schwab, The ALF (Algorithms for Lattice Fermions) project release 2.0. Documentation for the auxiliary-field quantum Monte Carlo code, SciPost Phys. Codebases , 1 (2022).

[3] N. Hatano and M. Suzuki, Finding exponential product formulas of higher orders, in *Quantum Annealing and Other Optimization Methods*, edited by A. Das and B. K. Chakrabarti (Springer Berlin Heidelberg, Berlin, Heidelberg, 2005) pp. 37–68.

[4] F. F. Assaad, M. Imada, and D. J. Scalapino, Charge and spin structures of a $d_{x^2-y^2}$ superconductor in the proximity of an antiferromagnetic mott insulator, Phys. Rev. B **56**, 15001 (1997).

[5] Y. Motome and M. Imada, A quantum monte carlo method and its applications to multi-orbital hubbard models, Journal of the Physical Society of Japan **66**, 1872 (1997), https://doi.org/10.1143/JPSJ.66.1872.

[6] L. Janssen and I. F. Herbut, Antiferromagnetic critical point on graphene's honeycomb lattice: A functional renormalization group approach, Phys. Rev. B **89**, 205403 (2014).

[7] H. K. Janssen, B. Schaub, and B. Schmittmann, New universal short-time scaling behaviour of critical relaxation processes, Zeitschrift für Physik B Condensed Matter **73**, 539 (1989).

[8] S. Yin, P. Mai, and F. Zhong, Universal short-time quantum critical dynamics in imaginary time, Phys. Rev. B **89**, 144115 (2014).

[9] B. Zheng, Generalized dynamic scaling for critical relaxations, Phys. Rev. Lett. **77**, 679 (1996).

[10] S. Zhang, S. Yin, and F. Zhong, Generalized dynamic scaling for quantum critical relaxation in imaginary time, Phys. Rev. E **90**, 042104 (2014).

[11] B. Zheng, Monte carlo simulations of short-time critical dynamics, International Journal of Modern Physics B **12**, 1419 (1998).

[12] Y.-R. Shu, S. Yin, and D.-X. Yao, Universal short-time quantum critical dynamics of finite-size systems, Phys. Rev. B **96**, 094304 (2017).

[13] Y. Otsuka, S. Yunoki, and S. Sorella, Universal quantum criticality in the metal-insulator transition of two-dimensional interacting dirac electrons, Phys. Rev. X **6**, 011029 (2016).

[14] K. Seki, Y. Otsuka, S. Yunoki, and S. Sorella, Fermi-liquid ground state of interacting dirac fermions in two dimensions, Phys. Rev. B **99**, 125145 (2019).

[15] T. C. Lang and A. M. Läuchli, Quantum monte carlo simulation of the chiral heisenberg gross-neveu-yukawa phase transition with a single dirac cone, Phys. Rev. Lett. **123**, 137602 (2019).

[16] S. M. Tabatabaei, A.-R. Negari, J. Maciejko, and A. Vaezi, Chiral ising gross-neveu criticality of a single dirac cone: A quantum monte carlo study, Phys. Rev. Lett. **128**, 225701 (2022).

[17] A. B. Migdal, The momentum distribution of interacting fermi particles, Soviet Phys. JETP **5**, (1957).